PERGAMON

International Journal of Heat and Mass Transfer 45 (2002) 679–689

International Journal of HEAT and MASS TRANSFER

www.elsevier.com/locate/ijhmt

Wall shear rate in the Taylor–Couette–Poiseuille flow at low axial Reynolds number

Eric Dumont [a,c], Francine Fayolle [a], Václav Sobolík [b], Jack Legrand [c,*]

[a] *Ecole Nationale Supérieure d'Ingénieurs des Techniques Agricoles et Alimentaires, GEPEA-UMR-MA 100, Rue de la Géraudière, BP 82225, 44322 Nantes cedex 3, France*

[b] *Laboratoire de Maîtrise des Technologies Agro-Industrielles, Université de La Rochelle, Pôle Sciences et Technologies, Avenue Michel Crépeau, 17042 La Rochelle cedex 01, France*

[c] *Université de Nantes, GEPEA-UMR-MA 100, CRTT, BP 406, 44602 Saint Nazaire cedex, France*

Received 20 October 2000; received in revised form 1 December 2000

Abstract

An experimental investigation was done by the use of visual observations and the electrochemical technique in order to study the appearance of hydrodynamic instabilities at low Re_{axg} in the gap between two coaxial cylinders, with radius ratio $R_r/R_s = 0.615$ and aspect ratio $L/e = 24$. A motor drove the inner cylinder and the outer cylinder was fixed. A Newtonian fluid (Emkarox HV45) and two non-Newtonian fluids (aqueous solutions of guar and CMC) have been used. The analysis of the evolution of the size of the Taylor vortices is carried out for $Re_{axg} < 4.0$. For $Re_{axg} < 2$ we showed that the vortices underwent a contraction phase up to $Ta_g \approx 80$, and a stretching phase for $Ta_g > 80$. For higher Re_{axg}, the contraction phase vanished and the vortices progressively stretched with increasing Ta_g. A dimensionless representation was also proposed for wall friction generalized to non-Newtonian fluids following the Ostwald law. © 2001 Elsevier Science Ltd. All rights reserved.

Keywords: Taylor vortices; Model fluids; Electrodiffusion diagnostics; Visual analysis; Wall shear rates

1. Introduction

Electrodiffusion probes mounted flush to a wall are largely used to measure the wall shear rate in order to study various hydrodynamic problems [1]. Thus, the well-known Taylor–Couette–Poiseuille flow is often studied using circular probes [2–4] or three-segment probes [5] and the results obtained allow us to understand more clearly the nature of the transition between laminar flow and fully developed turbulence.

Without axial flow ($Re_{axg} = 0$), the steady laminar flow in the annular space becomes unstable when the rotational speed of the inner cylinder is above a critical value. The other parameters (physical characteristics of the fluid and radii of the inner and outer cylinders), grouped in the Taylor number, also play a role in the instability. The first transition is characterized by the appearance of toroidal counter-rotating vortices, the vortex flow, which replace the original laminar Couette flow. In that case, the actual size of one vortex corresponds to the gap width. At higher rotating speeds, a second transition occurs where periodic azimuthal waves are superimposed on the vortices. Despite the number of published works (see [6]), the understanding of the inherent complexities of the Taylor–Couette system is far from being complete.

When an axial Poiseuille annular flow is superposed, the problem becomes even more complex: several different stable regimes appear in the Taylor–Couette–Poiseuille flow. According to the linear theory prediction, the axial flow has a stabilizing effect on the Couette flow [7,8] and the transition to vortex flow occurs for a critical value of Taylor number increasing with Re_{axg} [9]. Thus, the evolution of the flow structure is depending on the hydrodynamic parameters Re_{axg} and Ta_g. Only few

* Corresponding author. Tel.: +33-2 40 17 2633; fax: 33-2 40 17 2618.

E-mail address: jack.legrand@gepea.univ-nantes.fr (J. Legrand).

0017-9310/02/$ - see front matter © 2001 Elsevier Science Ltd. All rights reserved.
PII: S0017-9310(01)00183-1

Nomenclature

C_0	bulk concentration (mol m^{-3})
D	diffusion coefficient (m^2 s^{-1})
d	diameter of the microelectrode (m)
d_h	hydraulic diameter (m); $d_h = (d_s - d_r)$
d_r	rotor diameter (m)
d_s	stator diameter (m)
e	annular gap (m)
$\bar{f}$	friction factor (dimensionless)
$\bar{f}_g$	generalized friction factor (dimensionless)
f_m	frequency (Hz)
F	Faraday constant (A s mol^{-1})
I	limiting diffusion current (A)
K	consistency coefficient of the product (Ostwald law (Pa s^n))
k	mass transfer coefficient (m s^{-1})
L	stator length (m)
n	flow behavior index of the product (Ostwald law (dimensionless))
N	rotational speed (rev s^{-1})
Q	flow rate (m^3 s^{-1})
Re_{ax}	Reynolds number (dimensionless); $Re_{ax} = \rho U_d d_h/\mu$
Re_{axg}	generalized Reynolds number (dimensionless); $Re_{axg} = \rho U_d^{2-n} d_h^n/K$
R_r	inner cylinder radius (m)
R_s	outer cylinder radius (m)
$\bar{S}$	average wall shear rate (s^{-1})
S	local wall shear rate (s^{-1})
Sc	Schmidt number (dimensionless); $Sc = \mu/\rho D$
Sh	Sherwood number (dimensionless); $Sh = kd_h/D$
S_m	minimum wall shear rate at the inflow boundary in Taylor vortex (s^{-1})
S_M	maximum wall shear rate at the outflow boundary in Taylor vortex (s^{-1})
S_z	axial component of the wall shear rate (s^{-1})
S_θ	azimuthal component of the wall shear rate (s^{-1})
T	temperature (°C)
$Ta = \sqrt{\frac{R_s-R_r}{R_r}}\frac{\rho d_h}{2}\frac{(\omega R_r)}{\mu}$	Taylor number (dimensionless)
$Ta_g = \sqrt{\frac{R_s-R_r}{R_r}}\frac{\rho d_h^n}{2^n}\frac{(\omega R_r)^{2-n}}{K}$	generalized Taylor number (dimensionless)
Ta_c, Ta_{gc}	critical values of Taylor number (dimensionless)
U_d	mean axial velocity in the annular gap (m s^{-1})
z	number of electrons involved in the electrochemical reaction (dimensionless)
$\dot{\gamma}$	shear rate (s^{-1})
ω	rotating speed of the rotor (rad s^{-1})
ρ	density (kg m^{-3})
μ	dynamic viscosity for Newtonian fluid (Pa s)
Δ	size of a pair of Taylor vortices (m)

studies are dealing with the structure and/or the size of the vortices for small axial Reynolds number (Kataoka et al.: $4.5 < Re_{axg} < 260$ [2]; Legrand et al.: $30 < Re_{axg} < 770$ [3]; Nouar: $0.08 < Re_{axg} < 4.93$ [10]; Wronski and Jastrzebski: $0 < Re_{axg} < 200$ [4]). The use of more viscous Newtonian and non-Newtonian fluids allowed Giordano et al. [6] to obtain more information about the Taylor–Couette–Poiseuille flow for very low axial Reynolds number, $Re_{axg} < 1$. For pseudoplastic fluids following the power law model, it is established, theoretically [11,12] and experimentally [4], that the pseudoplasticity has a considerably destabilizing influence on the vortex flow in the initial range of the Reynolds number values ($Re_{axg} < 20$). A decrease of the flow index value, n, is accompanied by a decrease of the critical value of the Taylor number. The same effect has been observed for the flow index in circular Couette flow, $Re_{axg} = 0$ [13]. The destabilizing effect of pseudoplasticity vanishes in the range of the larger values of the axial Reynolds number.

In order to complete the information obtained on the evolution of the structure of the Taylor–Couette–Poiseuille flow and the size of the vortices for low values of Re_{axg}, this paper studies this flow for axial Reynolds numbers ranged from 0.01 to 4.0. The electrodiffusion method, based upon the measurement of the limiting diffusion current on the working electrode, is used to estimate the magnitude of the shear rate on the surface of the outer cylinder and to study the axial evolution of the spectral density of the fluctuations. Visualization experiments are also realized using a suspension of Kalliroscope AQ-1000 (Kalliroscope) in order to confirm the information given by the probes. The results obtained are discussed and compared with those of the literature, especially with the results obtained by Sobolík et al. [5] and Sobolík [14] who used three-segment electrodiffusion probes to measure the azimuthal and axial components of the shear rate in Taylor–Couette flow.

2. Experimental technique and working fluids

2.1. Electrochemical method

Wall shear rates were determined with the electrochemical method. The principle consists in measuring the electrical current I through a platinum microelectrode which results from a very fast redox reaction:

$Fe(CN_6)^{3-} + e^- \leftrightarrow Fe(CN_6)^{4-}$ with a large excess of supporting electrolyte K_2SO_4 in order to eliminate the migration current due to the electric field. A voltage difference ΔV is set between the probe (the working electrode) and a large counter electrode (the shaft). If ΔV is large enough, the ion concentration on the working electrode tends to zero and the current reaches a limit value I. This limiting current is fully controlled by diffusion. If the length of the microelectrode is very small in the flow direction, the concentration boundary layer on the electrode is as thin that we can assume a linear variation of the velocity in this sublayer. If the flow fluctuations are slow enough, the quasi-steady state hypothesis can be applied to relate the wall shear rate, S, to the limiting diffusion current, I [15]:

$$S = \left(\frac{1.477}{zF}\right)^3 \frac{I^3}{D^2 C_0^3 d^5}, \quad (1)$$

where z is the number of electrons involved in the redox reaction, F the Faraday constant, d the diameter of the circular microelectrode, C_0 the bulk concentration of the active ions and D the diffusion coefficient of these ions in solution.

2.2. Experimental apparatus

This work was carried out on the experimental apparatus consisting of an outer cylinder made of a PMMA tube and inner stainless steel cylinder (the shaft). The main dimensions are given in Table 1. A motor with controlled revolutions drove the shaft. Seven 0.4 mm diameter circular electrodiffusion probes were embedded in the wall of the outer cylinder. Calibration of the probes was performed using the well-defined shear Couette flow and the voltage-step transient experiment [16]. Visualizations and wall shear rates studies were carried out in isothermal conditions ($T = 25$°C; see [17]). The pilot plant included: a tank, a pump, the annular Couette test cell and an electromagnetic flowmeter (Endress Hauser). Data acquisition and experiment control were done by means of a numerical recorder (Digital AudioTape Tekelec RD-145T) with 16 channels allowing simultaneous recordings. The sampling frequency was equal to 6000 Hz. Each experiment was carried out in the following way: flow rate ($Q = 25$, 35 or 45 l h^{-1}), rotational speed of the shaft (N varies from 30 to 600 rpm) and fluid temperature ($T = 25$°C) at the inlet were adjusted to the desired values. For each rotational speed, the limiting diffusion currents from the microelectrodes were numerically recorded over 90 s (subcritical laminar flow) or over 150 s (vortex flow). Generalized axial Reynolds number (Re_{axg}) and generalized Taylor number (Ta_g) were used to characterize the flow pattern. Visual observations were carried out on Newtonian solutions with addition of a small amount of rheoscopic fluid Kalliroscope AQ-1000 from Kalliroscope. Kalliroscope fluid is a suspension of microscopic crystalline platelets which are oriented so as to align their larger dimensions parallel to the streamlines. In the presence of incident light, areas of varying orientation reflect different light intensities and their evolution and movement produce striking visual images of the streamlines.

Table 1
Geometrical characteristics of the annular space

Stator diameter (d_s)	0.13 m
Stator length (L)	0.60 m
Ratio (L/d_s)	4.61
Shaft diameter (d_r)	0.080 m
Ratio (d_r/d_s)	0.615
Gap $e = (d_s - d_r)/2$	0.025 m

3. Characteristics of the electrolytes

Three polymeric solutions were used to carry out the experiments: one Newtonian fluid and two power-law fluids. The viscosity measurements were performed at 25°C with a Couette rheometer TA Instrument AR 1000 with imposed torque.

Emkarox HV 45, from ICI, is a mixture of polypropylene glycol and polyethylene glycol. The dynamic viscosity of the pure products is equal to 3.7 Pa s at 25°C. The electrolyte was composed of a mixture of potassium ferricyanide, potassium ferrocyanide and potassium sulfate as supporting electrolyte. The viscosities of the different aqueous solutions are given in Table 2. We have also studied a low viscosity solution of polyethylene glycol 35000 (PEG).

Aqueous solutions of carboxymethylcellulose (CMC from SIGMA) have a pseudoplastic behavior. The non-Newtonian characteristics depend on the CMC concentration. CMC powder was progressively added in agitated cold water. After dissolution of carboxymethylcellulose sodium salt, potassium sulfate and potassium ferri- and ferrocyanide were added in the electrolyte. The rheological behavior was described by two different power-law equations according to the shear rate domains: (5–80 s^{-1}) and (50–1230 s^{-1}). The physical properties of CMC electrolyte are given in Table 3.

The preparation of guar gum solutions was similar to the one of CMC solutions, except that the guar gum dissolution was operated at 40°C. Two power-law equations were proposed to model the non-Newtonian behavior of guar gum solutions: one for $\dot{\gamma}$ between 2 and 20 s^{-1} and the second for $\dot{\gamma}$ between 10 and 1230 s^{-1}. The rheological data are summarized in Table 3.

The maximum values that Ta_g can reach according to the maximum rotational speed ($N = 10$ rpm) and the rheological behavior of each solution are presented in Table 4. Lastly, it can be mentioned that a special at-

Table 2
Physical properties of Emkarox HV45 solutions at 25°C

Solution	Water (w/w)	$K_3[Fe(CN)_6]$ (mol m^{-3})	$K_4[Fe(CN)_6]$ (mol m^{-3})	K_2SO_4 (mol m^{-3})	ρ (kg m^{-3})	μ (Pa s)	$D \times 10^{10}$ (m^2 s^{-1})
HV45-80	20%	5.327	5.327	106.5	1080	1.18	0.51
HV45-75	25%	5.304	5.304	127.3	1079	0.84	0.70
HV45-70	30%	5.283	5.283	158.5	1077	0.60	0.82
HV45-65	35%	5.262	5.262	210.5	1073	0.43	1.00
HV45-60	40%	5.241	5.241	209.6	1071	0.32	1.15
HV45-55	45%	5.220	5.220	229.7	1070	0.23	1.35
PEG	–	5.000	5.000	250.0	1058	0.04	3.50

Table 3
Physical properties of CMC and guar solutions at 25°C

						Shear rate domain $\dot{\gamma}$ (s^{-1})			
						5–80		50–1230	
Solution weight (%)	ρ (kg m^{-3})	$K_3[Fe(CN)_6]$ (mol m^{-3})	$K_4[Fe(CN)_6]$ (mol m^{-3})	K_2SO_4 (mol m^{-3})	D (10^{10} m^2 s^{-1})	n	K (Pa s^n)	n	K (Pa s^n)
CMC 0.5%	1046	5.0	5.0	300	7.50	0.85	0.11	0.73	0.16
CMC 0.7%	1071	5.0	5.0	500	7.50	0.78	0.36	0.65	0.63
CMC 0.9%	1047	5.0	5.0	300	7.50	0.70	1.05	0.55	1.98
CMC 1.0%	1047	4.0	4.0	300	7.50	0.66	1.64	0.51	3.02
CMC 1.1%	1048	4.0	4.0	300	7.50	0.62	2.49	0.48	4.44
						2–20		10–1230	
Guar 0.7%	1046	3.0	3.0	300	6.90	0.65	0.78	0.47	1.31
Guar 0.8%	1046	4.0	4.0	300	6.90	0.63	1.21	0.44	2.04
Guar 1.0%	1043	5.0	5.0	300	6.90	0.51	3.29	0.36	4.86
Guar 1.2%	1047	5.0	5.0	300	6.90	0.44	6.40	0.32	8.91

Table 4
Maximum Ta_g values for each working solution ($T = 25$°C)

Solution	Maximal Ta_g value ($N = 10$ rpm)	Solution	Maximal Ta_g value ($N = 10$ rpm)
		CMC 1.1%	32
HV45-80	11	CMC 1.0%	41
HV45-75	16	CMC 0.9%	52
HV45-70	22	CMC 0.7%	106
HV45-65	31	CMC 0.5%	282
HV45-60	42	Guar 1.2%	34
HV45-55	58	Guar 1.0%	51
PEG	328	Guar 0.8%	84
		Guar 0.7%	114

tention was devoted to the determination of the diffusion coefficients of ferricyanide ions, D, in these polymeric solutions [18].

4. Results and discussion

The time-evolution of the electrochemical current is directly related (Eq. (1)) to the flow regime [1–3]. Subcritical laminar, vortex or turbulent flow regimes induce different time-evolution of the wall velocity gradients and consequently different time-evolution of the diffusional limiting current. The flow stability investigation consists of determining the time dependence of the limiting current value I on the angular velocity ω of the inner cylinder for different axial flow rates. For low Taylor number, the value of I is nearly constant with the time (Fig. 1), which is interpreted as flow without vortices (subcritical laminar flow). When a critical value of rotational speed is reached, a sudden transformation of I appears. The limiting current value presents a periodical evolution (Fig. 1) attributed to the onset of the instability (vortex flow). The maximum value of I corresponds to the outflow boundary at the surface of the outer cylinder (maximum value of wall shear rate, see Fig. 2) while the minimum value corresponds to the inflow boundary (in that case, the wall shear rate has a minimum at the surface of the stator as shown in Fig. 2). This periodic evolution allows to determine the time required for a pair of vortices to axially flow in front of a reference probe and to calculate its size. This result is confirmed by visual experiments carried out with HV45 Emkarox solutions. It is found that the change in the limiting current evolution corresponds to the appearance of Taylor vortices (Figs. 2 and 4b). Toroidal vortices flow through the annulus without being disturbed by the axial flow. But it is noticed in Fig. 1 that the geometrical shape of the vortices differs according to the nature of the fluid used: vortices with Newtonian solution of PEG present a regular and smooth shape; vortices with non-Newtonian solution of CMC present some irregularities and vortices with non-Newtonian solution of guar are rather perturbed. These differences are probably related to the rheological properties of the solutions and could be due to non-explained viscoelastic effects (guar gum solutions). However, it is also noticed, for all the solutions, that the signal presents a plateau in the region of the maximum I-values (for instance: $Ta_g = 147$ for 0.5% CMC; $Ta_g = 97$ for 0.7% guar and $Ta_g = 82$ for PEG). This signal shape is due to a deformation of the vortices as shown in Fig. 3. The deformation becomes more pronounced with increasing Ta_g. In the case of Newtonian solutions, the increase of the deformation leads to the appearance of a local minimum in the plateau of maximum I-values (Fig. 1; PEG, $Ta_g = 197$ for instance). This local minimum could be attributed [2,19] to the generation of a new pair of small secondary vortices due to the separation of the boundary layer from the outer cylinder wall (Fig. 4b). These instabilities are not so pronounced on the records in the case of the non-Newtonian solutions (Fig. 1). Kataoka et al. [2] specify that the appearance of these secondary instabilities is related to a transition from laminar vortex flow to turbulent vortex flow. According to these

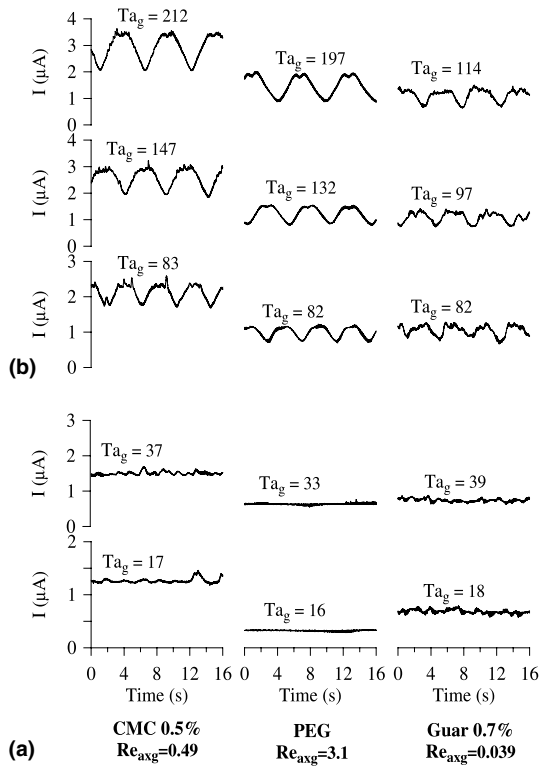

Fig. 1. Time-evolution of limiting diffusion current in an annulus for three different solutions: CMC (0.5%); PEG; guar (0.7%). Axial flow rate, $Q = 35$ l/h. (a) Subcritical laminar flow; (b) vortex flow.

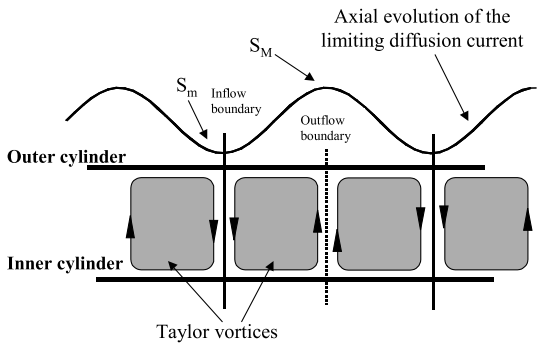

Fig. 2. Schematic representation of Taylor vortices.

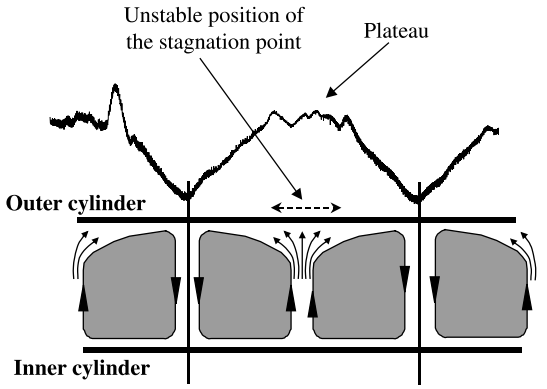

Fig. 3. Schematic representation of deformed Taylor vortices for a non-Newtonian CMC solution.

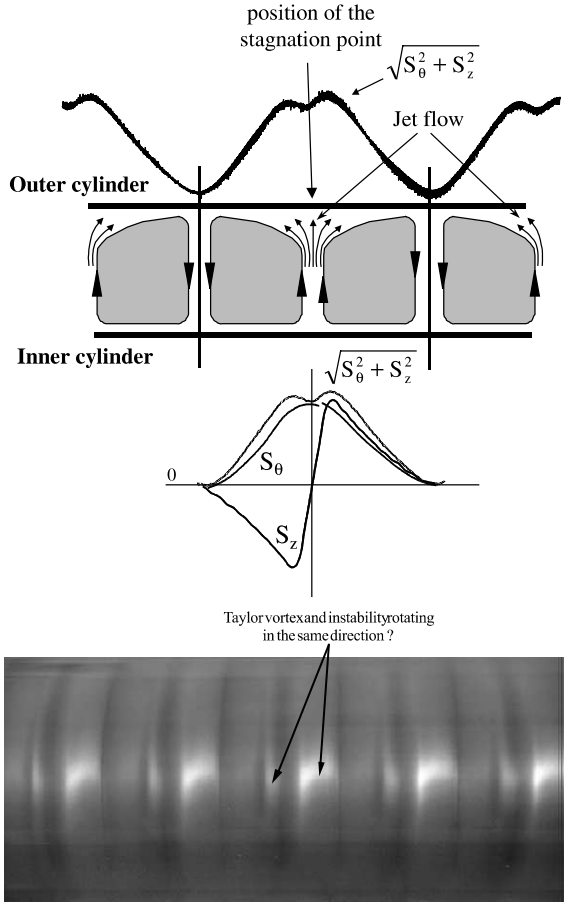

Fig. 4. (a) Schematic representation of deformed Taylor vortices for a Newtonian PEG solution; (b) View of Taylor vortex and instability rotating in the same direction for a Newtonian PEG solution ($Ta_g = 180$; $N = 10$ rpm; $Q = 0\ 1\ h^{-1}$).

authors, the transition gradually occurs over a relatively wide range of Taylor number $Ta_g = 500$–1000 for $R_r/R_s = 0.62$. When $Re_{axg} = 20$ for instance, the laminar vortex flow regime remains stable up to $Ta_g = 500$; at $Ta_g = 500$, the transition begins with the generation of disturbance near the inner rotating cylinder accompanied with small secondary vortices; when Ta_g exceeds 1000, the disturbance travels to the outer wall so that the flow reaches the turbulent vortex flow regime followed by the formation of small secondary vortices near the outer cylinder due to flow separation. After Wei et al. [20] and Lee et al. [21], these instabilities cannot be attributed to Görtler vortices. These authors have observed that the Görtler vortices first form at the inner cylinder for high Taylor numbers ($Ta/Ta_c > 20$). They have not observed Görtler vortices at the outer cylinder even at very high Taylor numbers. As the Taylor number is increased, the Görtler vortices become stronger and more numerous and contribute to the transition process to turbulence [20]. In our case, these secondary instabilities do not correspond to a change of flow regime as a turbulent flow regime (Fig. 4b) and it is surprising to observe these instabilities for Ta_g less than 200. One explanation could be found in the evolution of the different components of the wall shear rate on the outer wall. Sobolík et al. [5] have used a three-segment electrodiffusional probe in order to measure axial, S_z, and azimuthal, S_θ, components of the wall shear rate. At the separation line between two Taylor vortices, the outflow is similar to a jet flow (Fig. 4a) and because S_z is equal to zero, we speak about "stagnation point or line". Obviously, S_θ exhibits a maximum at this point. Around the stagnation point, the axial component of the wall shear, S_z, increases and the azimuthal component, S_θ, decreases. If the annular gap is larger, the thickness of the jet flow is increased (Fig. 4a) and Sobolík et al. [5] and Sobolík [14] have shown that the maximum of S_z moves in the direction of the stagnation point, while the maximum of S_θ remains at the stagnation point. Then, there is an axial shift of the position of the maximum of the resulting wall shear rate in a symmetrical way around the stagnation point. In our experimental study, we have only measured the resulting wall shear rate and the two maxima of S around the stagnation point (Fig. 4a) could be attributed to the axial shift of the maximum of the wall shear rate. Moreover, according to [5,14], presence of small counter-rotating vortices near the outer wall is excluded. If there were such vortices, the axial component of the wall shear should be equal to zero at three different axial positions along one vortex due to the three stagnation points. It was not observed by Sobolík et al. [5] (in particular Fig. 9 of [5]). The more fluctuating evolution of S_M signal (Fig. 3) for non-Newtonian fluids could be explained by the unstable position of the stagnation point.

The dependence of the generalized critical Taylor number on the flow index is shown in Fig. 5. The results on Ta_{gc} are compared with the numerical simulations made by Lockett et al. [13]. These simulations were

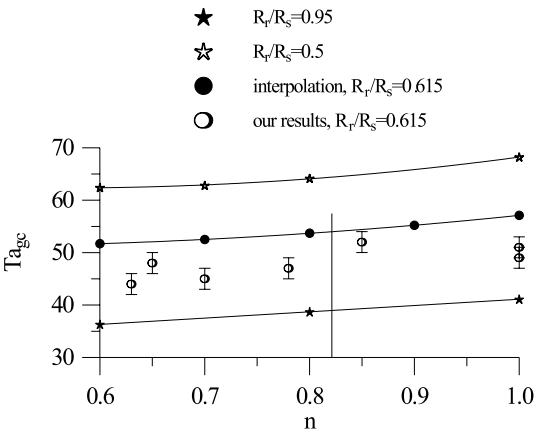

Fig. 5. Effect of flow behavior index on the critical generalized Taylor number.

published for $R_r/R_s = 0.95$ and 0.5 [13]. For $n = 1$, the dependence Ta_c vs. R_r/R_s is known, see for e.g., [14], and for $R_r/R_s = 0.615$ it gives $Ta_c = 57.1$. The values of Ta_{gc} for $R_r/R_s = 0.615$ and $n < 1$ were obtained by interpolation of the results of [13]. Experimentally, the evolution of Ta_{gc} with n is the same, i.e., Ta_{gc} grows with the flow index, but the values are lower than the prediction by interpolation. It is also true for $n = 1$, where the values of Ta_{gc} were confirmed by several authors for different values of R_r/R_s. The discrepancies are hardly to be explained by a finite aspect ratio, because $L/e = 24$ could be considered as infinite.

Analysis of the power density spectra of the fluctuations of the limiting diffusion current confirms the existence of organized structures (Taylor vortices) characterized by a main frequency (f_m) with high energy level and by secondary frequencies with low energy (Fig. 6). f_m is related with the axial movement of vortices and corresponds with the wavelength of a pair of Taylor vortices. Under the assumption that the axial phase velocity of vortices is equal to the mean axial velocity of the fluid, the f_m values allow to calculate the size of a pair of Taylor vortices (Δ) according to the following relation:

$$\Delta = \frac{Q}{\pi(R_s^2 - R_r^2)f_m}, \tag{2}$$

where Q is the flowrate and R_r and R_s the radius of the inner and outer cylinder respectively. Fig. 7 presents the evolution of the size of Taylor vortices (using the dimensionless ratio Δ/e and the annular gap $e = R_s - R_r$) with respect to Ta_g and Re_{axg} for three flow rates ($Q = 25$, 35 and 45 l/h). For $Re_{axg} < 1$ (in the case of guar and CMC solutions), this figure shows that the

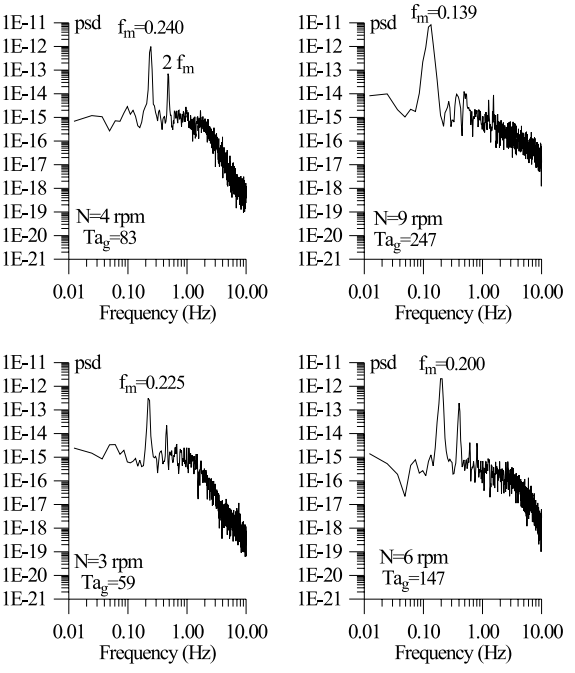

Fig. 6. Example of power spectral densities of the fluctuations of the limiting diffusion current in vortex flow (0.5% CMC solution; $Re_{axg} = 0.45$; $Q = 35$ l h^{-1}).

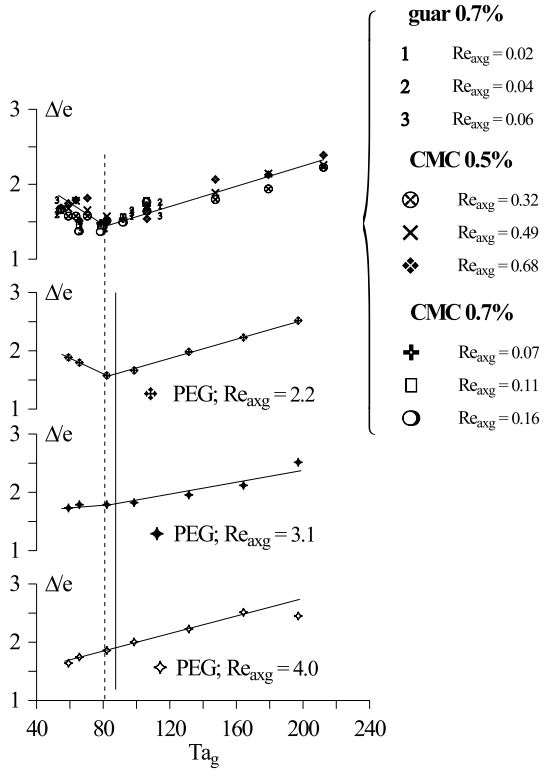

Fig. 7. Evolution of the vortex size with respect to Ta_g and Re_{axg} for Newtonian and non-Newtonian solutions.

value of $Ta_g \approx 80$ corresponds to a change of the evolution of the Δ/e ratio: contraction phase followed by a stretching one. Between $Ta_g \approx 45$ and $Ta_g \approx 80$, we observe a decrease of Δ/e ratio from 2 (value obtained without axial flow rate) to 1.5. Beyond $Ta_g \approx 80$, the Δ/e ratio increases up to 2.3. This change in the vortex size could be due to the axial flow rate. Indeed, the study of PEG results shows some differences in the evolution of the Δ/e ratio according to Re_{axg} values. For $Re_{axg} = 2.2$ ($Q = 25$ l/h), the scheme, contraction phase followed by stretching phase, is respected with a change for $Ta_g \approx 80$. For $Re_{axg} = 3.1$ ($Q = 35$ l/h), the contraction phase vanishes and the size of the Taylor vortices seems to be constant up to $Ta_g \approx 80$, then the Δ/e ratio increases for higher Ta_g values. Lastly, for $Re_{axg} = 4.0$ ($Q = 45$ l/h), it is not possible to distinguish a contraction phase: once they appear, the Taylor vortices are stretched as the rotating speed is increased. The same increase of the size of the Taylor vortices with Ta was described by Legrand et al. [3] for low axial Reynolds number ($Re_{ax} = 23$). Yet, it can be mentioned, in the specific case of PEG solution, that the Δ/e values is less than 2 when $Re_{axg} = 3.1$ and 4.0 and for small Ta_g values. It may be possible that a short contraction phase also exists in these cases as suggested hereafter by mass transfer analysis.

The use of the electrochemical method also allows measuring the time variation of wall shear rate on the body of the Taylor cells. Visual observations show that the outflow boundary (M) and the inflow boundary (m) bound the Taylor cells. S_M and S_m correspond to the value of the mean wall shear rate for respectively each boundary (Fig. 8). For the subcritical laminar flow, S is independent of the axial position of the microelectrode and linearly increases with Ta_g. At Ta_{gc}, when Taylor vortices appear, the value of S is higher for outflow and lower for inflow. When Ta_g increases, any value measured by probes is located between S_M and S_m (Fig. 8). For a given microelectrode, example of dimensionless representation of the mean wall shear rate, $\bar{S} \cong (S_M + S_m)/2$, is presented on Figs. 9–11. These representations allow detecting the transition between subcritical laminar flow and vortex flow and to verify the theoretical value of the ratio ($\bar{S}/N$) obtained from the Couette flow velocity profile for a power-law fluid (subcritical laminar flow):

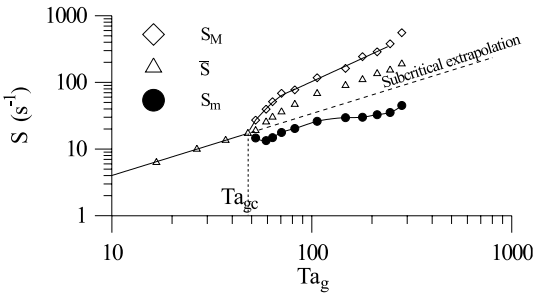

Fig. 8. Wall shear rates evolution with respect to Ta_g in annulus for a non-Newtonian solution of 0.5% CMC ($Re_{axg} = 0.49$; $Q = 35$ l h^{-1}).

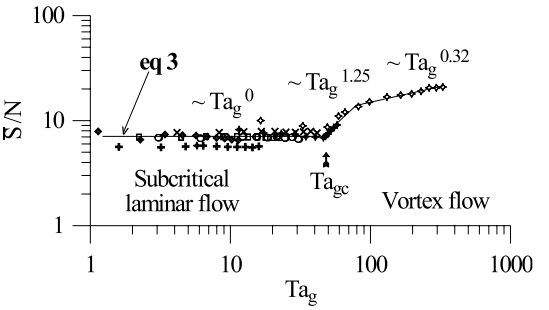

Fig. 9. Dimensionless representation of wall shear rates with respect to Ta_g in annulus for Newtonian solutions ($Q = 35$ l h^{-1}). (❖) HV45-80; (✣) HV45-75; (□) HV45-70; (❍) HV45-65; (×) HV45-60; (✦) HV45-55; (◇) PEG.

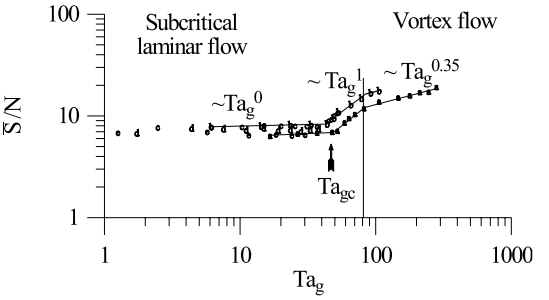

Fig. 10. Dimensionless representation of wall shear rates with respect to Ta_g in annulus for non-Newtonian CMC solutions ($Q = 35$ l h^{-1}). (a) 0.5% CMC; (b) 0.7% CMC; (c) 0.9% CMC; (d) 1.0% CMC; (e) 1.1% CMC.

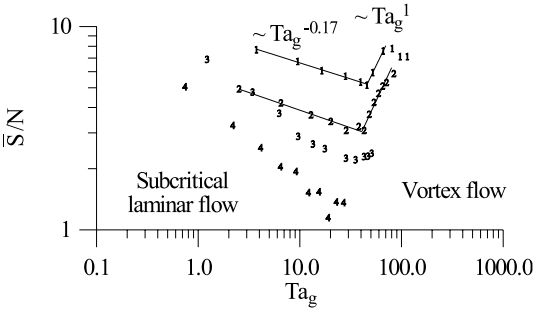

Fig. 11. Dimensionless representation of wall shear rates with respect to Ta_g in annulus for non-Newtonian guar solutions ($Q = 35$ l h^{-1}). (1) 0.7% guar; (2) 0.9% guar; (3) 1.0% guar; (4) 1.2% guar.

$$\frac{\bar{S}}{N} = \frac{4\pi}{n} \frac{R_r^{2/n}}{\left(R_s^{2/n} - R_r^{2/n}\right)}. \quad (3)$$

Figs. 9 and 10 clearly show that ($\bar{S}/N$) ratio varies with Ta_g following three distinctive zones:

1. $Ta_g <\approx 45$: $\bar{S}/N$ does not depend on Ta_g according to the circular Couette flow (Eq. (3)),
2. $\approx 45 < Ta_g <\approx 80$: $\bar{S}/N$ is increasing with Ta_g^1 for CMC solutions and $Ta_g^{1.25}$ for Newtonian solutions of Emkarox HV45 and flow regime corresponds to the vortex flow,
3. $Ta_g >\approx 80$: the effect of Ta_g on the evolution of $\bar{S}/N$ is reduced ($Ta_g^{0.35}$) but visual observations show that the Taylor vortex flow persists.

The evolution of $\bar{S}/N$ ratio is undeniably linked with the size of Taylor vortices. The change of the size of Taylor vortices (Fig. 7) implies a drastic change of shear rate evolution at the wall of the outer cylinder; the second zone ($\approx 45 < Ta_g <\approx 80$) corresponds to the contraction of the cells which leads to an important increase of the wall shear rate with Ta_g when the third zone ($Ta_g >\approx 80$) is characterized by a stretch of the cells which leads to a decrease of the effect of Ta_g on the wall shear rate. Fig. 11 shows that the evolution of $\bar{S}/N$ for the non-Newtonian guar gum solutions is different, especially in subcritical laminar flow ($Ta_g <\approx 45$) where $\bar{S}/N$ depends on Ta_g. The specific rheological behavior with non-explained viscoelastic effects of guar gum solutions [22] can be noted on Fig. 11.

The results presented in Figs. 9 and 10 agree with the conclusions proposed by Nouar [10] and by Maingonnat et al. [23]. These authors who studied the evolution of Nusselt number with respect to Ta_g for low Re_{axg} found the same three-phase scheme. This evolution of the flow pattern in three phases must be distinguished from that one in two phases based on the transition of the subcritical laminar flow to the vortex flow and conventionally described in the literature [4,24]. Existence of the three distinct zones with respect to Ta_g should be due to the axial flow conditions characterized by low Re_{axg} values. Indeed, Fig. 12 indicates that the second zone tends to vanish as Re_{axg} is increased. Furthermore, the analysis of the results presented by [4] confirms this tendency. These authors studied the evolution of $Sh/Sc^{0.33}$ ratio with respect to Ta_g in annular gap for different Re_{axg} values. For $Re_{axg} = 12$, three distinct zones can be observed and for larger Re_{axg} only two zones existed ($Sh/Sc^{0.33} \sim Ta_g^0$ in subcritical laminar flow and $Sh/Sc^{0.33} \sim Ta_g^{0.5}$ in vortex flow regime).

The evolution of mass transfer in three zones according to the development of the Taylor cells also appear when the generalized friction factor is plotted with respect to Ta_g (Fig. 13). For Newtonian fluids, the following relation (Cognet [25]), gives the dimensionless friction factor at the wall of the outer fixed cylinder:

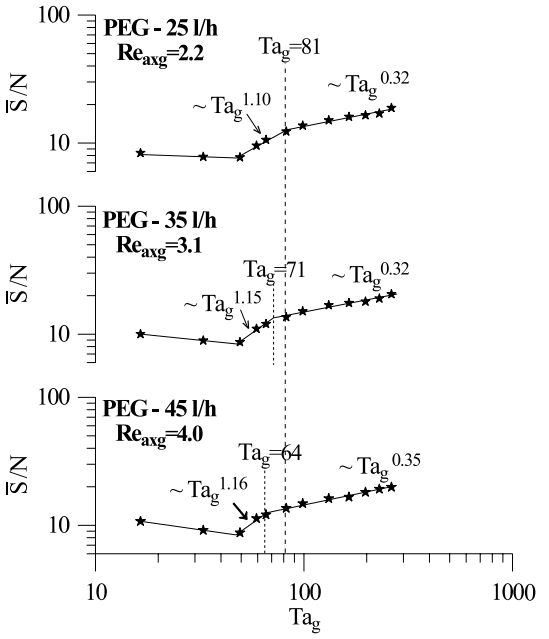

Fig. 12. Dimensionless representation of wall shear rates with respect to Ta_g and Re_{axg} for three different flow rates of a Newtonian PEG solution.

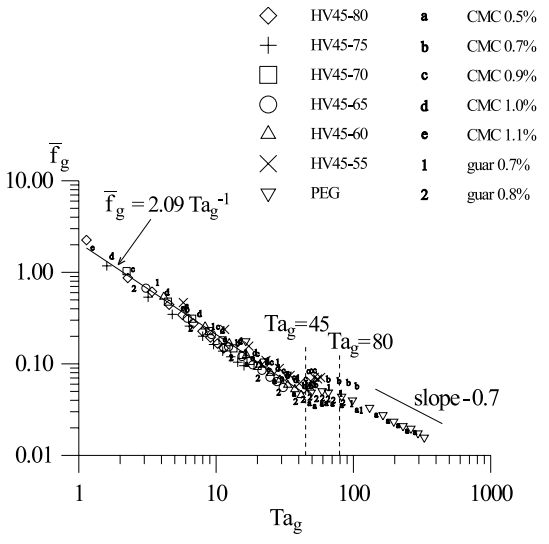

Fig. 13. Dimensionless representation of the friction factor at the wall of the outer stator with respect to Ta_g ($Q = 35\ \mathrm{l\ h^{-1}}$).

$$\bar{f} = \frac{\mu \bar{S}(R_s + R_r)}{\rho \sqrt{R_r(R_s - R_r)}(\omega R_r)^2}. \quad (4)$$

In laminar circular Couette flow without axial flow, the friction factor is theoretically given by relation (5):

$$\bar{f} = \frac{2}{Ta}. \quad (5)$$

According to relations (3) and (5), a dimensionless generalized friction factor at the wall of the outer cylinder for the Couette flow can be written as:

$$\bar{f}_g = \frac{Kn\bar{S}\left(R_s^{2/n} + R_r^{2/n}\right)}{\rho R_r^{((4-3n)/2n)}\left(R_s - R_r\right)^{((1+2n)/2)}\left(\omega R_r\right)^{3-n}}. \quad (6)$$

Fig. 13 groups our results obtained with all working fluids except 1.0% and 1.2% non-Newtonian guar solutions. We experimentally found the slope predicted by the theory for circular Couette flow without axial flow. Thus, Fig. 13 shows that the effects of axial flow for $Re_{axg} < 5$ do not influence the evolution of the friction factor which corresponds to the one of Couette flow. The use of the dimensionless numbers: $\bar{f}_g$ and Ta_g, allows representing the evolution of wall shear rates measured for Newtonian and non-Newtonian fluids in laminar flow following an unique dimensionless form of the Eq. (3). Therefore, this representation allows to distinguish the transition between subcritical laminar and vortex laminar flow regimes and to suspect that a decrease of the flow index value (for CMC solutions) is accompanied by a decrease of the critical value of the Taylor number according to the conclusion of Wronski and Jastrzebski [4].

5. Conclusion

Couette–Taylor–Poiseuille flow of Newtonian and non-Newtonian fluids in annular gap has been investigated for low axial Reynolds number ($Re_{axg} < 4.0$). Visualization and analysis of the limiting diffusion current measured by the electrodiffusion probes allowed us to emphasize the deformation of Taylor vortices. For large gap, this deformation modifies the distribution of the wall shear rate at the outer wall, which is explained with the axial evolution of the axial and azimuthal components of the wall shear rate.

Our results also show that for $Re_{axg} < 2$, the increase of the rotational speed leads to a change of the size of the Taylor cells which fundamentally influences the evolution of the wall shear rate. For Ta_g going from 45 to 80, there is a contraction of the vortices and $\bar{S}/N$ ratio is proportional to $Ta_g^{1-1.25}$. For Ta_g greater than 80, a stretch of vortices is observed and in this case, $\bar{S}/N$ ratio is proportional to $Ta_g^{0.33-0.35}$. For higher values of the axial Reynolds number, the contraction phase tends to vanish.

A single dimensionless representation of the friction factor for Newtonian fluids and non-Newtonian fluids obeying to the Ostwald law has been proposed. This representation, which allows to compare directly the results obtained with the different power-law fluids used, shows the dependence of the stability of the Taylor flow regime with respect to the flow index (n) at low axial Reynolds number.

References

[1] T.J. Hanratty, Use of the polarographic method to measure wall shear stress, J. Appl. Electrochem. 21 (1991) 1038–1046.
[2] K. Kataoka, H. Doi, T. Komai, Heat/mass transfer in Taylor vortex flow with constant axial flow rates, Int. J. Heat Mass Transfer 20 (1977) 57–63.
[3] J. Legrand, F. Coeuret, M. Billon, Structure dynamique et transfert de matière liquide-paroi dans le cas de l'écoulement laminaire tourbillonnaire de Couette-Poiseuille, Int. J. Heat Mass Transfer 26 (1983) 1075–1085.
[4] S. Wronski, M. Jastrzebski, Experimental investigations of the stability limit of the helical flow of pseudoplastic liquids, Rheol. Acta 29 (1990) 453–461.
[5] V. Sobolík, B. Benabes, G. Cognet, Study of Taylor–Couette flow using a three-segment electrodiffusion probe, J. Appl. Electrochem. 25 (1995) 441–449.
[6] R.C. Giordano, R.L.C. Giordano, D.M.F. Prazeres, C.L. Cooney, Analysis of a Taylor–Poiseuille vortex flow reactor – I: flow patterns and mass transfer characteristics, Chem. Eng. Sci. 20 (1998) 3635–3652.
[7] S. Chandrasekhar, Hydrodynamic and Hydromagnetic stability, Clarendon Press, Oxford, 1961.
[8] H.A. Snyder, Proc. Roy. Soc. London 265 (1962) 198.
[9] R.C. DiPrima, The stability of a viscous fluids between rotating cylinders with an axial flow, J. Fluid. Mech. 9 (1960) 621–630.
[10] C. Nouar, Convection thermique pour un fluide rhéofluidifiant. Cas de l'écoulement de Couette–Poiseuille, thesis, Nancy, 1986.
[11] S. Wronski, M. Jastrzebski, The stability of the helical flow of pseudoplastic liquids in a narrow annular gap with a rotating inner cylinder, Rheol. Acta 29 (1990) 442–452.
[12] S. Yim, N. Titchener-Hooker, P. Ayazi Shamlou, Proc. of First European Congress on Chem. Eng. Florence 3 (1997) 1709.
[13] T.J. Lockett, S.M. Richardson, W.J. Worraker, The stability of inelastic non-Newtonian fluids in Couette flow between concentric cylinder: a finite-element study, J. Non-Newtonian Fluid. Mech. 43 (1992) 165–177.
[14] V. Sobolík, Electrochemical study of Taylor–Couette flow by limiting diffusion current method, Collect. Czech. Chem. 64 (1999) 1193–1210.
[15] L.P. Reiss, T.J. Hanratty, An experimental study of the unsteady nature of the viscous sublayer, AIChE J. 8 (2) (1963) 154–160.
[16] V. Sobolík, J. Tihon, O. Wein, K. Wichterle, Calibration of electrodiffusion friction probes using a voltage-step transient, J. Appl. Electrochem. 28 (1998) 329–335.
[17] E. Dumont, Caractérisation des écoulements et des frottements pariétaux dans un échangeur de chaleur à surface raclée, thesis, Nantes, 1999.
[18] J. Legrand, E. Dumont, J. Comiti, F. Fayolle, Diffusion coefficients of ferricyanide ions in polymeric solutions. Comparison of different experimental methods, Electrochim. Acta 45 (2000) 1791–1803.
[19] A. Bouabdallah, Instabilités et turbulence dans l'écoulement de Taylor–Couette. Transitions par évolution spectrale et phénomènes d'interactions instabilités – turbulence, thesis, Nancy, 1980.

[20] T. Wei, E.M. Kline, S.H.-K. Lee, S. Wooddruff, Görtler vortex formation at the inner cylinder in Taylor–Couette flow, J. Fluid Mech. 245 (1992) 47–68.
[21] S.H.-K. Lee, S. Sengupta, T. Wei, Effect of polymer additives on Görtler vortices in Taylor–Couette flow, J. Fluid Mech. 282 (1995) 115–129.
[22] E. Dickinson, D. Lorient, Food macromolecules and colloids, Proceedings ENSBANA, Bourgogne University, Dijon, France, 23–25 march 1994, The Royal Society of Chemistry, Cambridge, 1995.
[23] J.F. Maingonnat, J.C. Leuliet, T. Benezech, Modélisation de la vitesse de cisaillement apparente dans un échangeur de chaleur à surface raclée. Application aux performances thermiques avec des produits non-Newtoniens, Revue Générale de Thermique 306–307 (1987) 381–385.
[24] J. Legrand, F. Coeuret, Transfert de matière global liquide-paroi pour des écoulements associant tourbillons de Taylor et circulation axiale forcée, Int. J. Heat Mass Transfer 25 (3) (1982) 345–351.
[25] G. Cognet, Utilisation de la polarographie pour l'étude de l'écoulement de Couette, J. de Mécanique 10 (1) (1971) 65–90.